Uniformity Scan in the Inner Wheel and the crack between the two wheels ($\eta = 2.5$) of the Electromagnetic End-cap Calorimeter

P. Barrillon, F. Djama, L. Hinz, P. Pralavorio
CPPM, CNRS/IN2P3 - Univ. Méditerranée, Marseille - France

ATL-LARG-2001-014
23 August 2001

Abstract

The Module 0 of the electromagnetic end-cap calorimeter was assembled and tested with electron beams in 1999. This note presents the uniformity and the energy resolution obtained in the inner wheel and the crack region (η=2.5). A constant term of $\sim 0.6\%$ (excluding the crack), compatible with the expectation, is obtained in the inner wheel. Crack effect is mainly sensitive in the region $\eta = 2.5 \pm 0.01$.

1 Introduction

The module 0 of the liquid argon electromagnetic end-cap calorimeter (EMEC) [1] was intensively tested during 3 weeks at CERN, in 1999. In order to accommodate the accordion geometry in the end-cap region, the detector needed to be divided in two concentric wheels: *i*) the outer ($\eta = [1.4, 2.5]$), and *ii*) the inner ($\eta = [2.5, 3.2]$). In both wheels, gaps and absorber waves angle vary continuously, whereas high voltage settings vary by step. The goal of this study, based on about 3 millions events[1], is to present the uniformity and the resolution of the calorimeter in the inner wheel ($\eta = [2.5, 3.2]$) and the crack region ($\eta = [2.45, 2.55]$), after correcting for HV and geometry effects. Results obtained in the outer wheel ($\eta = [1.4, 2.5]$) are discussed elsewhere [2].

This note is organized as follow. Generalities about the inner wheel are given in section 2. Section 3 reviews the results obtained for the uniformity scan analyses in the inner wheel, and section 4 the study of the crack region as well as a detailed comparison with simulation. Conclusions are given in section 5.

2 Generalities on the Inner Wheel

Since a detailed description of the inner wheel can be found in [1], only the main features and a description of the stacking are recalled in this section.

2.1 EMEC Inner wheel description

2.1.1 Granularity

Contrary to the outer wheel, the main goal of the η region above 2.5 is to detect missing energy in LHC collisions. Therefore a coarser granularity and only two samplings are necessary in the inner wheel [3]:

- The middle sampling (S2): the cell width size in η is constant ($\Delta\eta = 0.1$) and 4 adjacent electrodes with the same η cell are summed in ϕ ($\Delta\phi = 0.1$). S2 has a 24 X_0 constant depth, corresponding to the sum of S1 and S2 in the outer wheel.
- The back sampling (S3): the cell size is identical to S2 and its depth increases with η from 4 to 12 X_0.

The granularity of the inner wheel, as well as in the outer wheel near the crack region ([2.4,2.5]), is summarized in Table 1. We should notice that in module 0, the inner wheel was complete (ϕ range between 0.0 and 0.785) while the outer wheel was half equipped with electrodes (ϕ range between 0.196 and 0.589).

[1] There were two test periods: a short one (4 days with a 200 GeV electron beam) and a longer one (two weeks with 10-180 GeV positron beams) where uniformity scans were performed.

	$\eta \times \phi$ range	
	[2.4,2.5]×[0.196,0.589]	[2.5,3.2]×[0.0,0.785]
S1	0.025×0.1	–
	(212-215)×(2-5)	–
S2	0.025×0.025	0.1×0.1
	(40-43)×(8-23)	(44-50)×(0-7)
S3	0.050×0.025	0.1×0.1
	(18-19)×(8-23)	(20-26)×(0-7)

Table 1: *$\Delta\eta \times \Delta\phi$ of calorimeter cells in the crack region and the inner wheel. $(\eta_{cell}) \times (\phi_{cell})$ cell ranges are given for each region.*

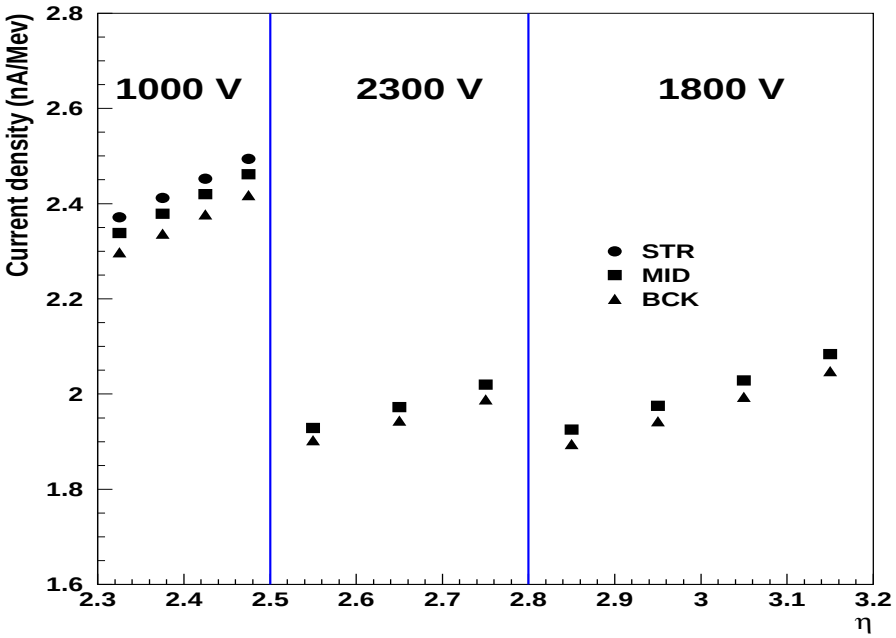

Figure 1: *Current density in nA/MeV, as a function of η [4] in one outer wheel HV zone ($2.3 < \eta < 2.5$) and for the inner wheel ($2.5 < \eta < 3.2$). The high voltage values set on the detector are indicated. Vertical lines represent the separation between high voltage sectors.*

2.1.2 High voltage

The calorimeter response, *i.e.* the peak current (I_{peak}), can be written as [4]:

$$I_{peak} \sim \frac{f_{samp}}{g} \times E_{field}^{0.3} \sim \frac{f_{samp}}{g^{1.3}} \times U^{0.3} \tag{1}$$

where g is the gap between electrodes and absorbers, f_{samp} the sampling fraction and U, the high voltage (HV). Because of the end-cap geometry, g decreases with η from roughly 3 to 2 mm in the inner wheel (in the outer wheel before the crack region, $g \sim 1$ mm). As the absorber's thickness is constant per wheel[2], the sampling fraction follows the same variation. Consequently, for a given constant electric field (E_{field}) the dependence of f_{samp} and g with η almost cancels out.

However, in practice, high voltages are set by projective HV sectors (2 in the inner wheel), first approximation to get a constant electric field. The expected calorimeter response from simulation is shown in Figure 1, as well as the high voltage settings. The current density (i_0^E) increases linearly with η inside each HV sector l, with a slope h_i^l, which does not depend on the sampling i, $h_1^l = h_2^l = h_3^l = h^l$:

$$I_{peak} = i_0^E \times E_{el} \ , \quad i_0^E = I_0^E \times \left(1 + h_i^l \cdot (\eta - \eta_{center}^l) + O(\eta - \eta_{center}^l)^2\right) \tag{2}$$

where η_{center}^l is the center of the considered high voltage sector, E_{el} the energy of the incident electron. For safety reasons, high voltage settings have to be less than 2500 V at liquid argon temperature. Therefore, it was not possible to obtain the same current density on both wheels and I_0^E is 1.97 and 2.45 nA/MeV in the inner and outer wheel respectively [4].

2.2 Inner Wheel stacking and cabling

A complete inner wheel containing 32 absorbers and 31 electrodes was assembled in parallel[3] with the stacking of the outer wheel, already described in [2]. Each absorber, with 6 waves accordion shape, is fixed on 4 indexing rings located at outer and inner radii of the inner wheel (front and back side).

A typical shape of the sagitta measured for one absorber is shown in Figure 2a. A parabolic shape is observed with a peak on the 4^{th} wave. Therefore the gap, between absorber and electrode, is greater than the nominal value in S2. Thanks to the fixation on the structure, S3 is less affected.

To ease comparison with results presented hereafter, we now consider the sagitta of the 4^{th} wave averaged over 4 absorbers (S2 cell size in ϕ). Figure 2b shows its evolution along the stacking. The sagging amplitude is constantly increasing, with a slope of about 0.45 mm per cell. It was attributed to the spacer net thickness and cured for the production modules (spacer fabrication is improved and net thickness is reduced). This problem could affect the uniformity of the detector response.

[2]The absorber's thickness is 1.7 mm in the inner wheel and 2.2 mm in the outer wheel.

[3]In the inner wheel, one absorber is stacked each three absorbers in the outer wheel.

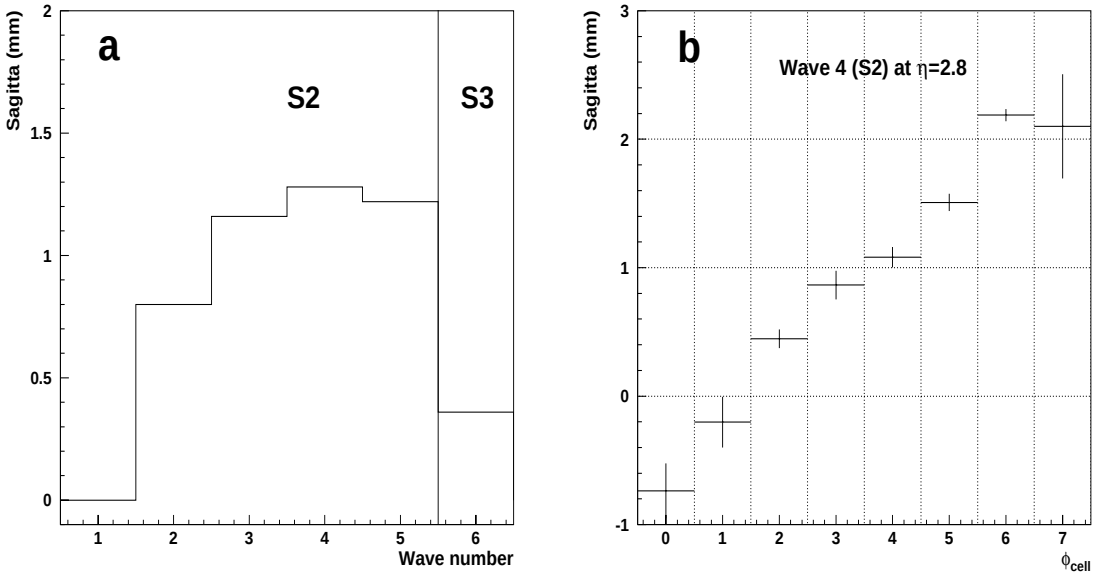

Figure 2: *a) Typical sagitta shape as a function of the wave number at* $\eta = 2.8$ *(vertical full line represent the separation between S2 and S3) and b)* 4^{th} *wave sagitta, averaged over 4 absorbers, as a function of* ϕ_{cell}*, at* $\eta = 2.8$.

Cold electronics (summing and mother boards) were then plugged in the detector. Dedicated studies [5] demonstrated that these boards are responsible of high inductive crosstalk (1-2%), and thus possible source of non uniformity.

No problems were observed during the high voltage tests performed at warm during and after the stacking. Cold HV tests in the cryostat at CERN were also positive.

3 Uniformity scans in the inner wheel

The EMEC module 0 was tested in the CERN North Area. A 100 GeV positron beam, described in more detail in [6], is used to scan the detector in two directions: *i)* η, in the range [2.45,3.1] for one ϕ line ($\phi = 0.3375$) and *ii)* ϕ, in the range [0.1,0.7] for 3 η lines ($\eta = 2.65, 2.85, 2.95$). Except in the crack region, pions are vetoed at the analysis level using the information of scintillator counter located behind the detector[4].

3.1 Data analysis

We used EMTB software [7] to access test beam data. The shaped and digitized signals are then processed (after pedestal subtraction) with the optimal filtering technique [8] using:

[4]Muons are vetoed at the trigger level.

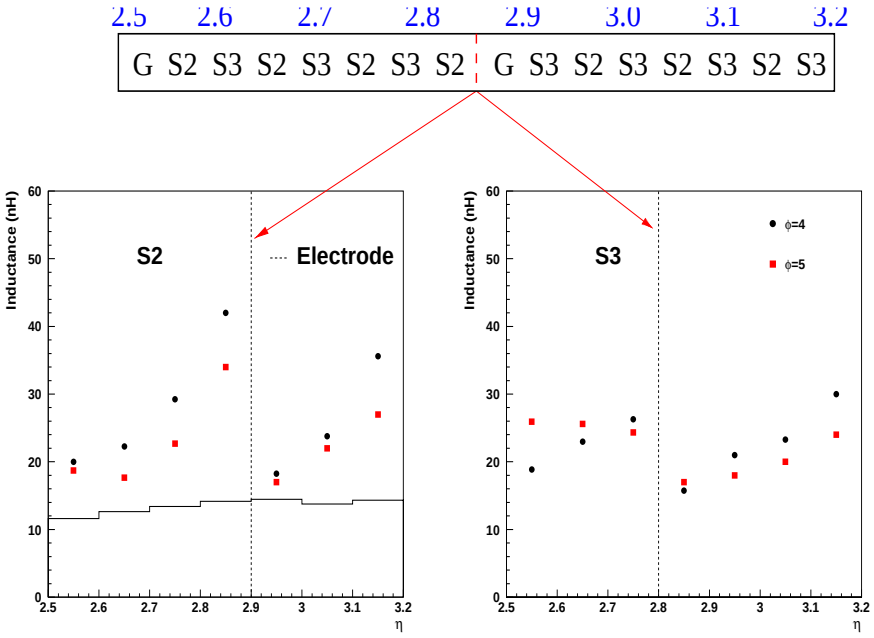

Figure 3: *Inductance measured in S2 and S3 with an RLC meter, after taking out the mother boards. The full histogram shows the theoretical electrode inductance [11]. Vertical dashed lines represent the separation between summing boards. The inner wheel connectors are also represented where G is the ground connection.*

- for calibration: a tabulation of the signal shape [8];
- for physics: a sigmoïd sums using neural network fit [9].

The maximum of signal amplitude (A_{max} in ADC counts) is obtained, calibrated and finally converted in DAC units. To correct for the different inductance values seen by calibration and physics signals, a factor $\frac{M^i_{cal}}{M^i_{phy}}$ is computed [10] and applied to each cell i. Figure 3 shows the measured inductances[5] as a function of η, for S2 and S3 at 2 different ϕ. Two effects are observed:

1. A variation in ϕ due to difference in summing board strip line length. This effect is less than 8 nH and will affect the ϕ uniformity.

2. A variation in η related to the insufficient grounding, especially true for the S2 cell at $\eta = 2.85$ and the S3 cell at $\eta = 3.15$. This effect can amount up to 20 nH.

Hardware solutions proposed to solve these two effects for the production modules are described in [2].

Finally the cell energy (E_i) in the sampling i is defined as:

$$E_i = \gamma_i \times DAC \times \frac{M^i_{cal}}{M^i_{phy}} \ , \tag{3}$$

[5]These values are obtained with a RLC-meter after unplugging the mother boards.

	$\Delta\eta_{cell} \times \Delta\phi_{cell}$		
	Inner Wheel scan	Crack Scan ($\eta = [2.45, 2.55]$)	
		Outer Wheel	Inner Wheel
Strips	–	4×1	–
Middle	3×3	4×5	2×3
Back	1×1	1×1	1×1

Table 2: *On the left, cluster size per layer around cell with maximum energy deposit for the inner wheel scan. On the right, cluster size per layer, kept constant along the crack scan, in the outer and inner wheel.*

where γ is a global conversion coefficient applied to obtain GeV. It can be expressed as:

$$\gamma_i = V_{Count}^{DAC} \times \frac{1}{I_0^E} \times \frac{1}{R_i} \tag{4}$$

where V_{Count}^{DAC} is the value of DAC counts in units of voltage (3.81×10^4 nV/DAC), R_i is the equivalent resistance of the calibration system on the mother boards and I_0^E is the current density, cf. Equation (2). Numerically, it gives:

$$\gamma_2 = \gamma = 38.8\ MeV\ , \quad \gamma_3 = \frac{\gamma}{2} \tag{5}$$

in the inner wheel and

$$\gamma_2 = \gamma = 31.2\ MeV\ , \quad \gamma_3 = \frac{\gamma}{2} \tag{6}$$

in the outer wheel. In this analysis, the γ factor computed with the test beam data (cf. section 3.2) is 8 % less compare to the expected value. A similar effect is observed in the outer wheel [2].

3.1.1 High voltage correction

The different stepped high voltage settings (cf. Figure 1) are sources of energy dispersion. To correct for this effect, weights are applied on each cell depending on η, sampling and HV sector. This is detailed in section 3.2.

3.1.2 Clustering

Clusters are constructed in each sampling and their energies (E_{Si}) are summed to compute the total energy (E_{tot}). Table 2 shows the various sizes chosen for the inner wheel and the crack scan.

For uniformity scans in the inner wheel, the cluster is formed around the cell with maximum energy deposit (as in the outer wheel scans), whereas for the crack analysis, the cluster is fixed all along the scan. With the choice of a rather large cluster in the latter case, we will only be sensitive to the crack effect (no lateral leakage). In S3, because of

the cross-talk [5] and the low value of energy deposit, we take the cell in regard of the S2 cell with maximum energy deposit.

η and ϕ barycenters are computed in S2 as:

$$\eta_{bar}^{S2} = \sum_{j=1}^{N_j}\sum_{k=1}^{N_k} \frac{E_2(\eta_j,\phi_k)\times\eta_j}{E_{S2}} \ , \quad \phi_{bar}^{S2} = \sum_{j=1}^{N_j}\sum_{k=1}^{N_k} \frac{E_2(\eta_j,\phi_k)\times\phi_k}{E_{S2}} \tag{7}$$

where $N_j \times N_k$ is the number of cells in the cluster. No attempt were made to correct for the barycenter bias (S-shapes).

3.1.3 Geometrical corrections

Once the total energy is obtained, two geometrical corrections are applied. The η lateral leakage, caused by the finite size of the cluster, and the ϕ-modulation, induced by the accordion geometry. In both case, the corrected energy is computed as:

$$E_{tot}^{corr} = \frac{E_{tot}(s)}{f(s)} \ , \ s \ = \ \eta \ , \phi \tag{8}$$

where f is the fitted function which parameterizes the normalized energy variation as a function of s. The section 3.2 shows how these corrections are obtained.

3.2 η scan

A complete η scan of the inner wheel, centered on $\phi = 0.3375$, was performed. Because the S2 cell size (from 5.8 cm at $\eta = 2.55$ to 3 cm at $\eta = 3.15$) is larger than the beam size (about 1.5 cm in η), 4 runs per S2 cell were recorded[6], *i.e.* $\Delta\eta = 0.025$. This allows us to completely cover the region $\eta = [2.6, 3.1]$.

Figure 4a shows the mean value of the total energy as a function of η. The γ coefficient, calculated to obtain a mean response of 100 GeV over the scanned zone, is 0.0359. In this Figure, the energy dispersion mainly comes from the stepped high voltage.

3.2.1 High voltage correction

To correct for this non uniformity, we apply weights (w_i^l) on each cell depending on η, the sampling (Si) and the HV sector (l):

$$w_i^l(\eta_j) = 1 + \alpha_i^l \cdot (\eta_j - \eta_{center}^l) + \vartheta(\eta_j - \eta_{center}^l)^2 \tag{9}$$

η_{center}^l being the center of the considered high voltage sector. In the case of simulation, α_i^l can be computed directly from Figure 1.

As for the outer wheel([2]), we make the following hypothesis (also predicted by simulation):

$$\alpha^l = \alpha_2^l = \alpha_3^l \tag{10}$$

[6] A total of 19 runs with 30000 events each were taken.

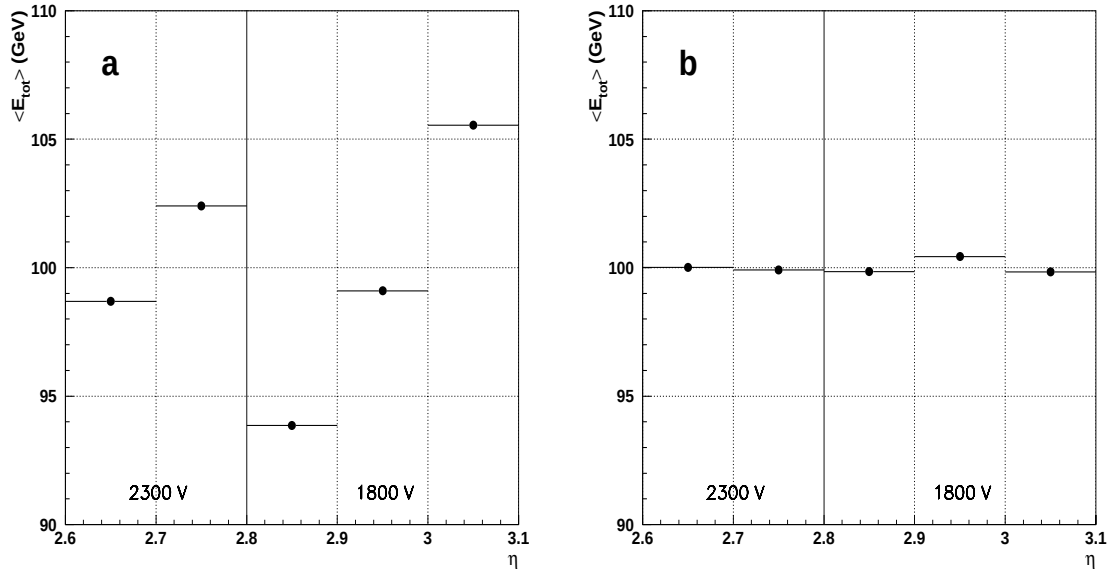

Figure 4: *Total energy as a function of η: a) before and b) after high voltage corrections. Inductance corrections are applied. Vertical full line corresponds to high voltage sectors separation, and dotted ones to cell boundaries.*

To compensate for the difference in the detector response per HV sector, global factors, β^l:

$$\beta^l = \frac{E_{beam}}{E^l_{tot}} \tag{11}$$

are computed. E^l_{tot} is the mean value of total energy per HV sector l, and E_{beam} is the beam energy (100 GeV, here).

We minimize the total energy dispersion per high voltage sector using α^l parameters, in a two steps process. For the first iteration, α^l coefficients extracted from simulation are taken as input. A second iteration is then performed with the new α^l parameters as input. Convergence within few % is achieved after a second iteration. Table 3 gives parameters obtained for simulation and data. Errors indicate the variation between the output of first and second iterations.

Figure 4b shows the mean value of the total energy as a function of η after high voltage corrections are applied. The energy dispersion is now clearly reduced compare to Figure 4a.

3.2.2 η leakage correction

Figure 5a shows the total energy as a function of the η barycenter computed in S2, after high voltage corrections. Expected parabola shape in each cell, due to lateral leakage, is

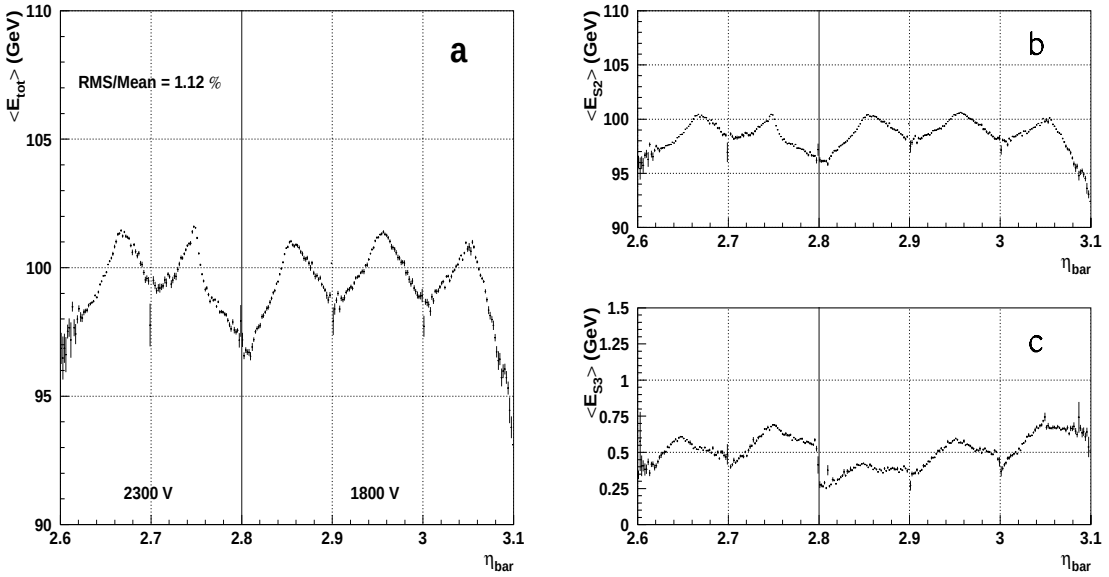

Figure 5: *a) Total and b-c) S2 and S3 energies as a function of η barycenter in S2. Vertical full line corresponds to high voltage sector separation and dotted ones to separations between cells.*

severely degraded. This can be explained by the non-correction of S-shapes. As a result, the energy dispersion is of the order of 1.12%. Figures 5b-c show the energy for middle and back sampling. We can observe that around 99% of the total energy is deposited in S2 and that energy in S3 is not well corrected for the high voltage effect.

From simulation, we expect the total energy variation as a function of η barycenter to be parametrized as:

$$F_1(\eta_{bar}) = C_0 \cdot f_1(\eta_{bar}) = C_0 \cdot \left(1 + C_1 \cdot \left[(\eta_{bar} - \eta_{S2}^{center}) - C_2\right]^2\right) \tag{12}$$

where C_0 is the maximum of the parabola (in our case, it basically corresponds to the beam energy), C_1 its curvature (sensitive to the cluster size) and C_2 the position of the

η	Simulation		Data	
range	α	β	α	β
2.5-2.8	-0.23	1	-0.60 ± 0.01	1.02
2.8-3.2	-0.26	1	-0.75 ± 0.02	0.98

Table 3: *α and β coefficients in the 2 HV sectors scanned, for simulation and data. Errors indicates the variation between the output of first and second iterations.*

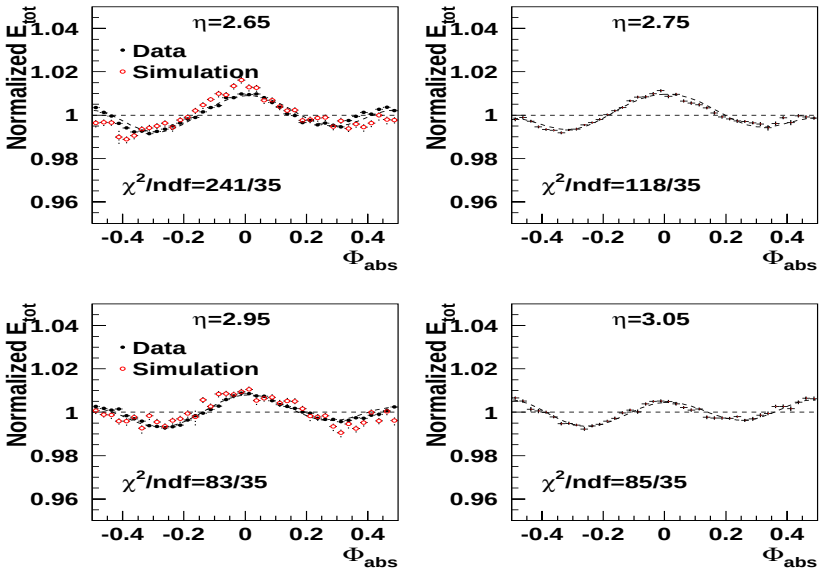

Figure 6: *ϕ-modulation in absorber unit for 4 η values. A cluster 3×3 has been used in S2. The curve is a function (Fourier series) used to correct for ϕ-modulation. Results from simulation with charge collection are shown at $\eta = 2.65$ and $\eta = 2.95$.*

maximum with respect to the center of the S2 cell (η_{S2}^{center}).

According to the distorted parabola shapes seen in Figure 5a, this function is clearly not satisfactory for test beam data. However, if this correction is applied the energy dispersion is improved to 0.61 %.

3.2.3 ϕ-modulation

Figure 6 shows the ϕ-modulation in absorber unit (ϕ_{abs}) at four different η values. The amplitude is constant over η, around 2%. This dependence of the total energy as a function of ϕ barycenter can be parametrized with Fourier series:

$$F_2(\phi_{abs}) = a_0 \cdot f_2(\phi_{abs}) = a_0 \cdot \left(1 + \sum_{i=1}^{3} a_i \cdot \cos(2\pi i \phi_{abs}) + b_1 \cdot \sin(2\pi\phi_{abs})\right) \quad (13)$$

where a_0 is the mean total energy, a_i are the even coefficients. b_1 is an odd coefficient which takes into account calorimeter local defects. At $\eta = 2.65$ and $\eta = 2.95$, a comparison with simulation (including charge collection) is presented and good agreement is found with the data.

Fitted parameters of ϕ-modulation versus η are shown in Figure 7. a_1 and a_2 cosine terms can be fitted with a parabola. The third cosine term (a_3) is compatible with 0. Therefore only two cosine parameters are necessary to fit ϕ-modulation in the inner wheel. The sine term (b_1) is small indicating that calorimeter defects are well under control.

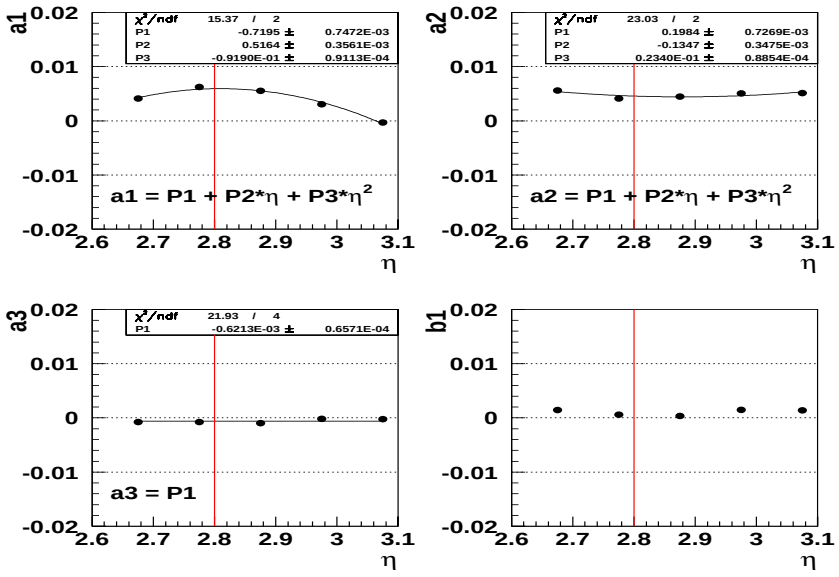

Figure 7: *Fitted parameters of ϕ-modulation versus η. a_1 and a_2 are adjusted with a parabola. a_3 is compatible with 0.*

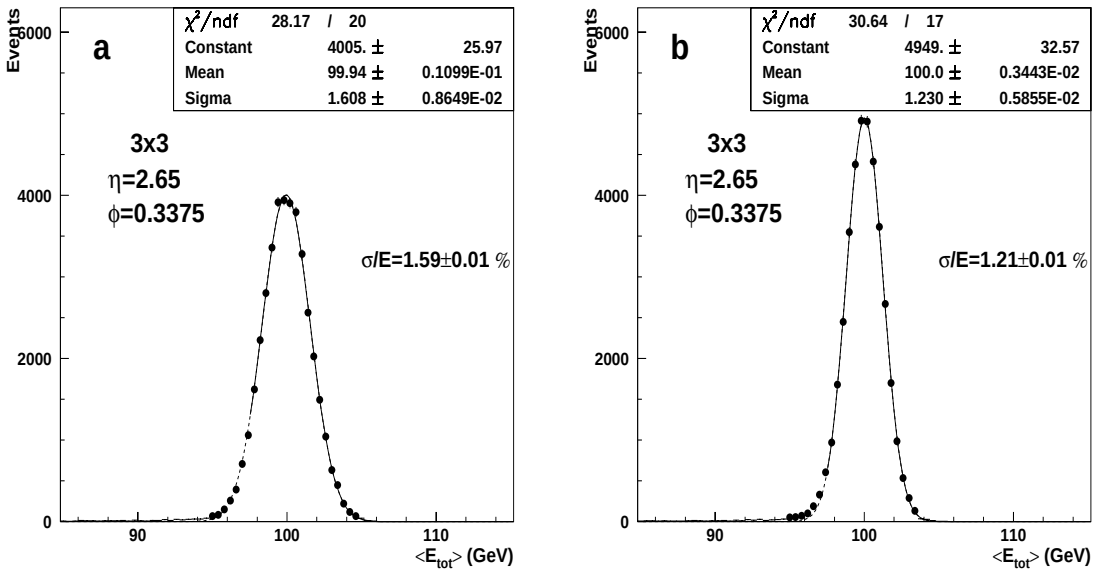

Figure 8: *Total energy distribution at $\eta = 2.65$ ($\phi = 0.34$) for a 3×3 cluster in S2, a) before and b) after geometrical corrections. $\frac{\sigma}{E}$ indicated on the two plots is the energy resolution after beam spread subtraction.*

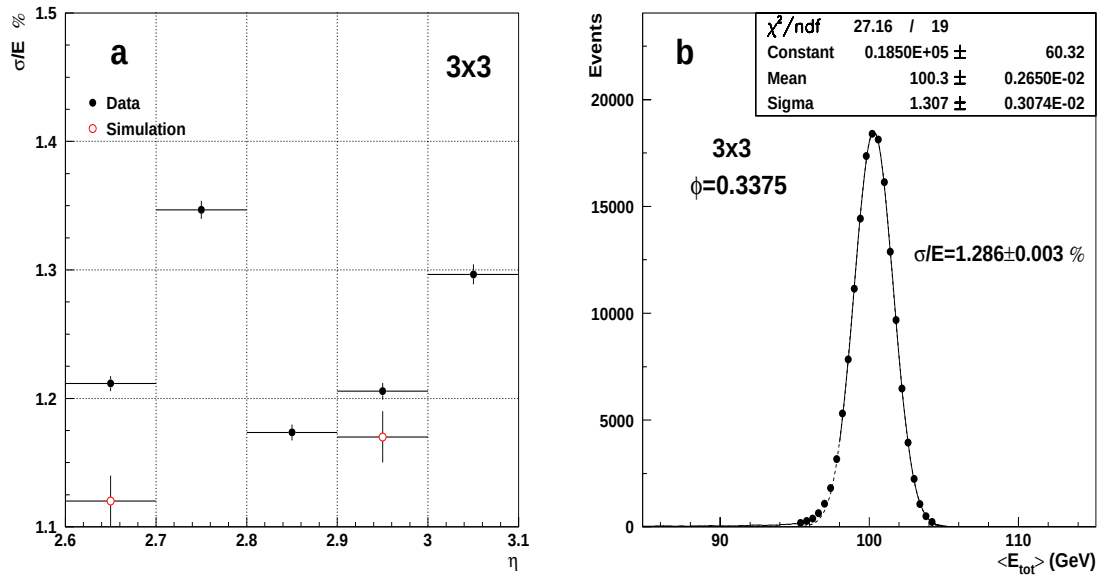

Figure 9: *a) Energy resolution versus η (simulation is present at η=2.65 and η=2.95), after subtraction of the beam spread, and b) total energy distribution over the η scan. A cluster of 3×3 is used in S2.*

3.2.4 Energy resolution

Figure 8 shows the total energy distribution at $\eta = 2.65$ before and after geometrical corrections. The energy resolution improves from 1.6% to 1.21% (improvement of 24%). Figure 9a shows the energy resolution versus η for test beam data, after beam spread subtraction, and for simulation (2 points). Except for $\eta = 2.75$ (η dependence is abnormal) and $\eta = 3.05$ (close to the calorimeter edge), the energy resolution is below 1.25% in good agreement with simulation. Figure 9b shows the total energy distribution over the η scan. A resolution of 1.29% is obtained. Subtracting quadratiquely the sampling term (1.05% [12]) and the noise term (0.5%[7]) a constant term of 0.55% is obtained for the η scan.

[7]We are using only the medium gain.

3.3 ϕ scans

Overall ϕ scans were performed for three η lines : 2.65, 2.85 and 2.95. To obtain a complete ϕ coverage, the main constraint comes from the beam size (about 2 cm in ϕ) to be compared to the ϕ cell size in S2 (from 6.7 cm at η=2.55 to 3.5 cm at η=3.15). Thus 3 runs[8] were taken per S2 cell. The total energy, as a function of ϕ barycenter, is shown in Figure 10 for the 3 scans. For $\phi_{bar} < 1$ and $\phi_{bar} > 6$, part of the electromagnetic shower starts to develop out of the detector. Consequently, we observe a decrease of the energy in these regions (labelled 1 and 3 on Figure 10), especially in the latter one, completely scanned. Therefore, for uniformity purposes, we will concentrate on zone 2 which covers 4 ϕ cells ($\phi_{cell} = 2 - 5$), where the value of mean energy is constant. In each cell, four ϕ-modulation are observed, corresponding to the number of absorbers. A global parabola effect is also present and can be explained by the shower leakage out of the 3×3 S2 cluster. This leakage is smaller than for ϕ_{cell}=1 and 6 because of the possibility of shower particles back scattering in the cluster. Before correcting these two effects, the measured energy dispersion is of the order of 0.6-0.7%, depending on η.

Averaged ϕ lateral leakage can be parametrized as:

$$F_1(\phi_{bar}) = C_0 \cdot f_1(\phi_{bar}) = C_0 \cdot \left(1 + C_1 \cdot \left[(\phi_{bar} - \phi_{S2}^{center}) - C_2\right]^2\right) \qquad (14)$$

Once this effect is corrected, an average ϕ-modulation over the four ϕ cells (16 absorbers) can be performed. Figures 11a-c show the result in absorber unit, after normalization, for the 3 ϕ scans. The fitted parameter values are comparable with the ones extracted in the η scan, cf. section 3.2. Figures 11d-f show the total energy as a function of ϕ barycenter after both corrections are applied. The energy dispersion is reduced by a factor of more than 1.5 compared to Figure 10, leading up to about 0.5% at $\eta = 2.65$, and 0.4% at $\eta = 2.85$ and $\eta = 2.95$. As a comparison, an energy dispersion of about 0.3% is obtained in the outer wheel at $\eta \sim 2.2$ with a 3×5 cluster in S2.

The final energy resolution as a function of ϕ_{cell}, after correcting for all geometrical effects (including η lateral leakage) and subtracting the beam spread, is shown in Figure 12a. The energy resolution is around 1.2% for ϕ_{cell} = 2-4. The degradation of energy resolution observed at $\phi_{cell} = 5$ may come from an increase of the sagitta in this region (cf. Figure 2b). Figure 12b shows the total energy distribution over the three ϕ scans for ϕ_{cell} =2-5, after all corrections are applied. The energy resolution is 1.306%. If we subtract the contributions from the average sampling term (1.05%) and the noise term (0.5%), the constant term obtained is 0.59%.

4 Crack study

The crack region ($\eta = [2.45, 2.55]$) was scanned at $\phi = 0.3375$, the only zone not affected by HV problems (the power was not supplied on the HV zone [$\eta = 2.3 - 2.5$, $\phi = 0.4 - 0.6$] because a short circuit was detected at cold). A total of 18 runs of 30000 events were taken each $\Delta\eta \sim 0.006$. The Figure 13 shows a detailed schematic view of the crack region.

[8]For one ϕ scan, this represents 18 runs with 30000 events each.

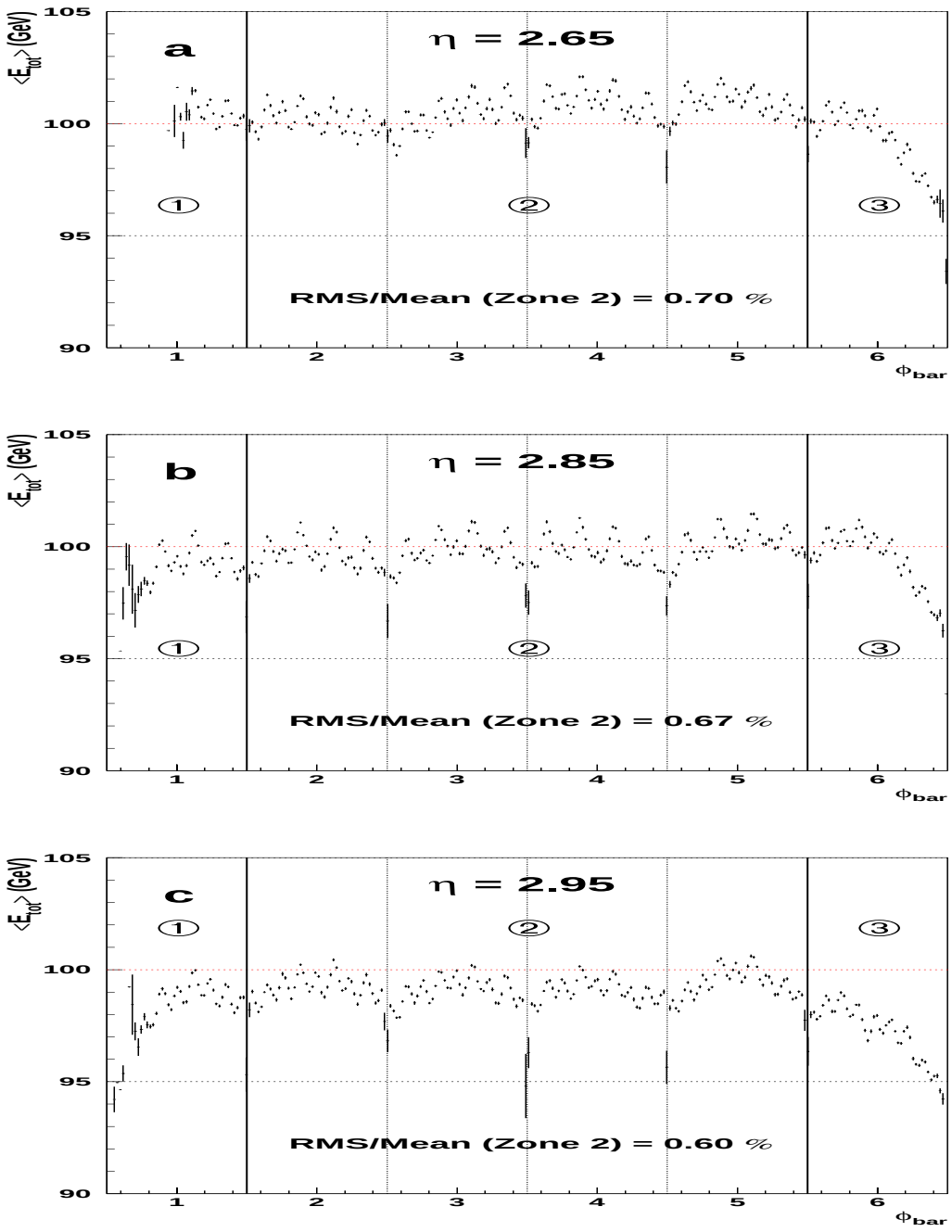

Figure 10: *Total energy as a function of ϕ barycenter computed in S2, for the three positions in η : 2.65 (a), 2.85 (b) and 2.95 (c). Solid vertical lines represent separation between zones of interest, and dotted separation between cells.*

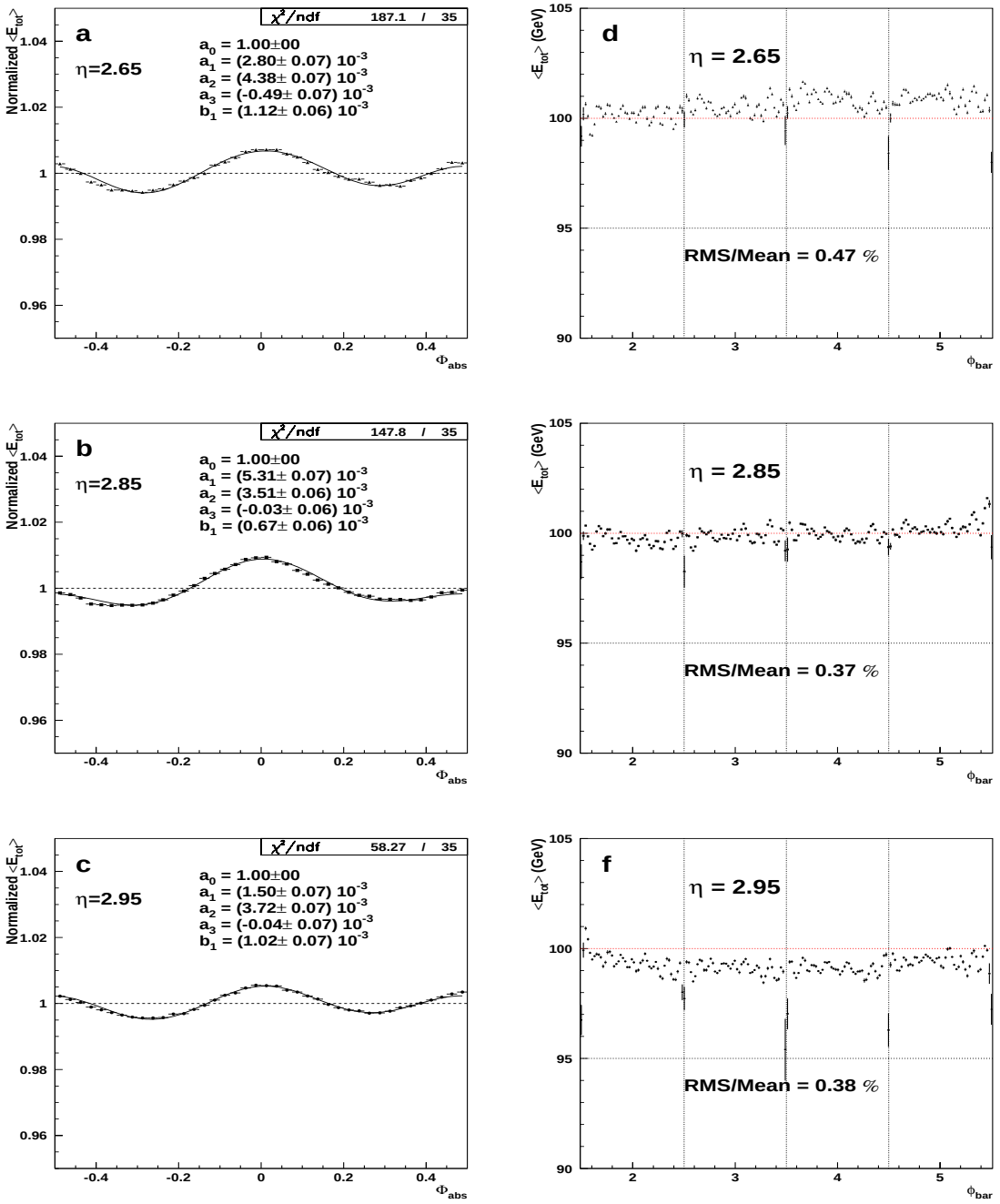

Figure 11: *a-c) average ϕ-modulation and d-f) total energy versus ϕ barycenter in S2 after all corrections, for the three phi scans.*

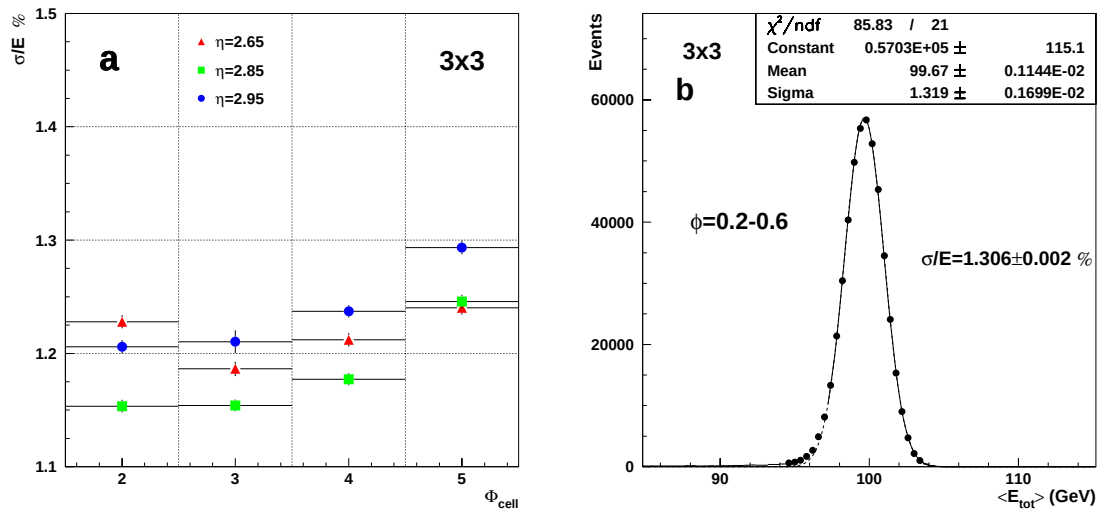

Figure 12: *a) Energy resolutions and b) total energy distributions over the three ϕ scans. A 3×3 cluster is chosen in S2.*

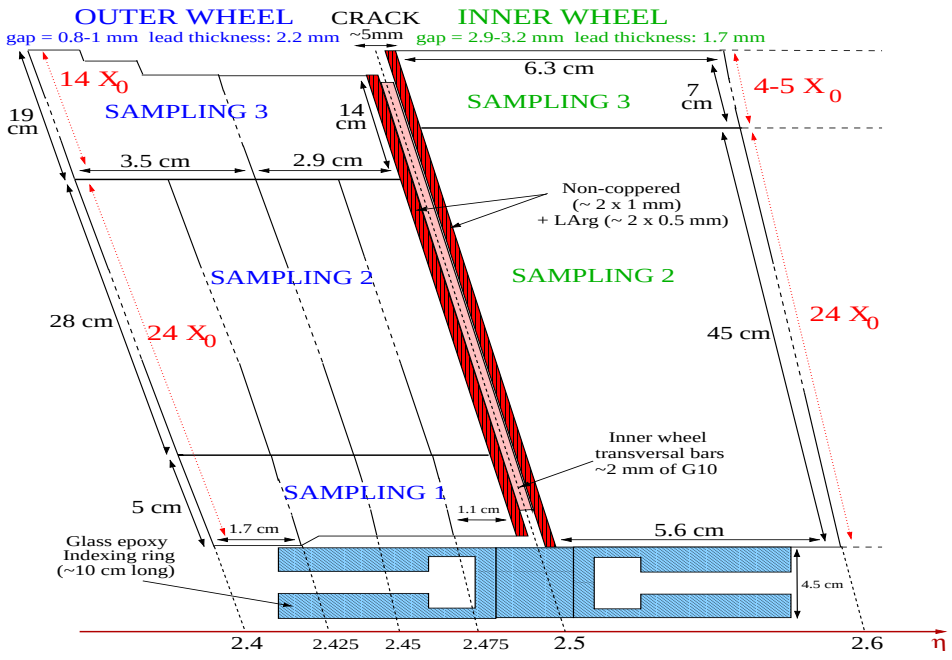

Figure 13: *Schematic view of the crack region between η=2.4 and η=2.6. The cell size is represented, as well as the dimension of each sampling.*

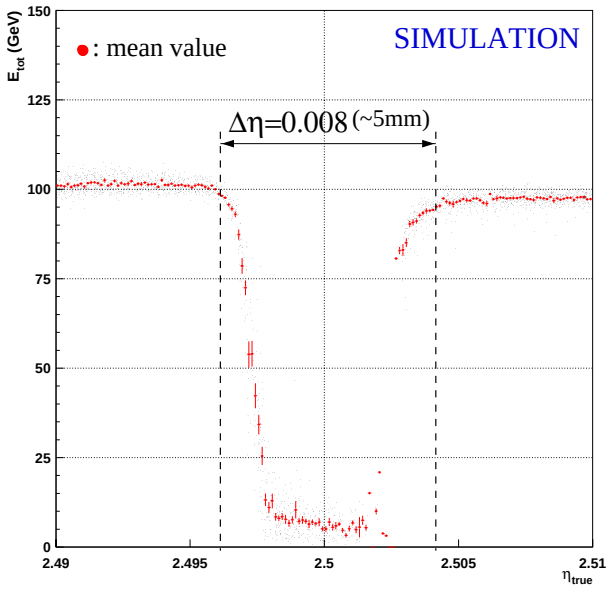

Figure 14: *Simulation of total energy (black point) and mean total energy (full circles) as a function of the true η value for the range $\eta = [2.49, 2.51]$.*

The interleave ($\sim$ 3 mm) between the two wheels is filled with the G10 transversal bars of the inner wheel absorbers and with liquid argon.Therefore the crack has roughly 3 X_0 in depth, to be compared to the 38 X_0 of the outer wheel (at $\eta = 2.49$) and the 28 X_0 of the inner wheel (at $\eta = 2.51$). It should be noticed that inner and outer wheel electrodes are not coppered on 0.5 mm near $\eta = 2.5$, which will affect the charge collection in this region.

A quantitative estimation of the electron energy loss in this region is provided by simulation (with charge collection). For this purpose, a projective 100 GeV electron beam was used. Figure 14 shows the total energy as a function of the true value of η (η_{true}) in the region $\eta = [2.49, 2.51]$. Only a small zone of 5 mm, corresponding to $\eta = 2.5 \pm^{0.004}_{0.004}$, is affected by the presence of the crack. At the center of this region, 90% of the total energy is lost.

In the following, to be mainly sensitive to the crack effect, we chose a constant cluster in between the two wheels as illustrated in Figure 15[9]. The global scale γ differs for the two wheels, cf. section 3.1. In the inner one, we choose the same γ as in the inner wheel scan. In the outer wheel, as no η scan was performed in the region η =2.3-2.5, we estimate γ from the zone η=2.45-2.475.

[9]See also table 2.

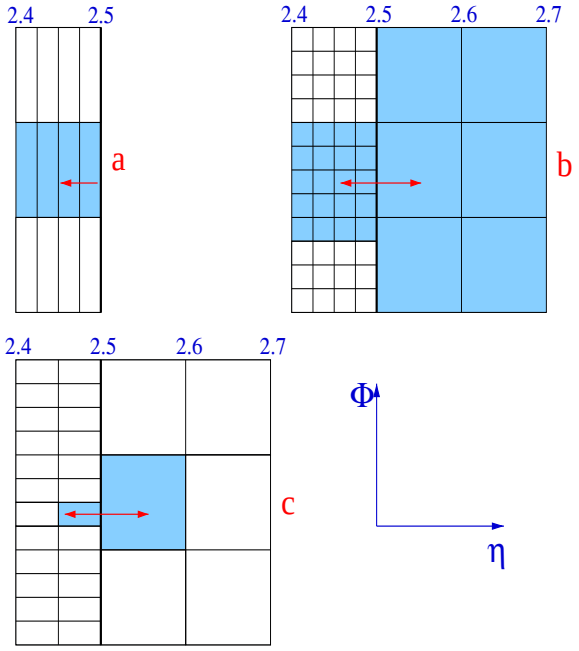

Figure 15: *Cluster choice for the front (a), the middle (b) and the back (c) sampling. Shaded zones correspond to the chosen clusters, the thick solid line the crack and the thin ones separations between neighboring cells. Arrows delimit the scanned region.*

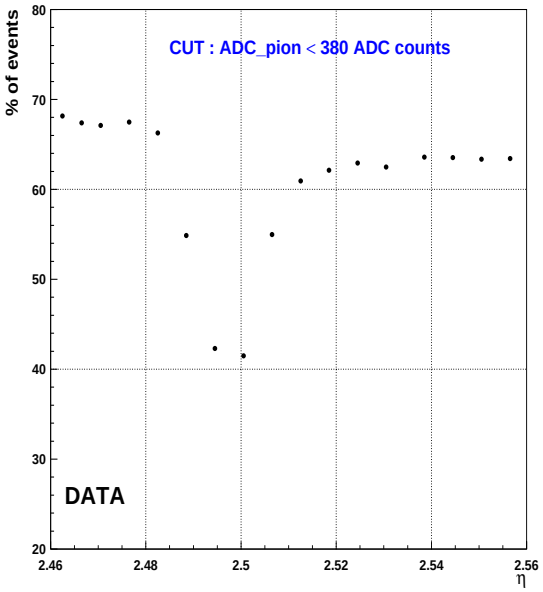

Figure 16: *Percentage of events, after cut on pions ($ADC_{pion} < 380$), versus η.*

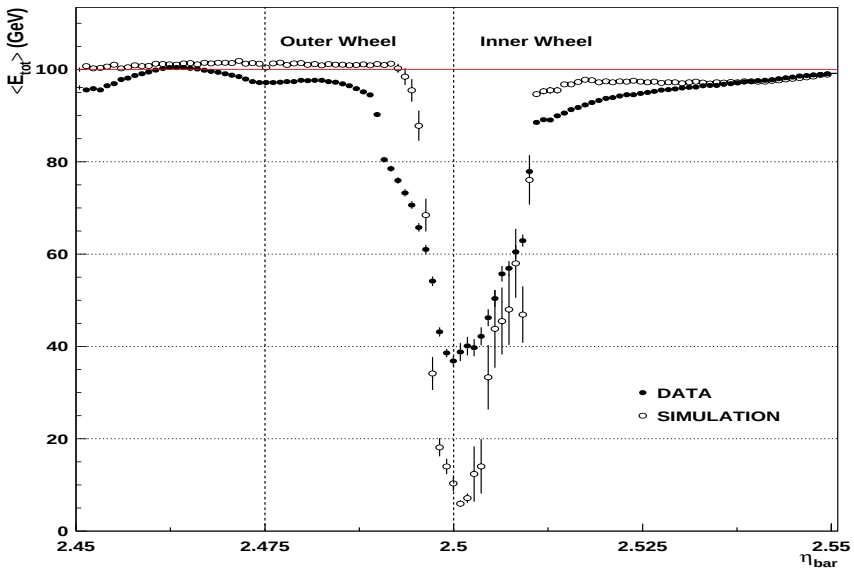

Figure 17: *Total energy as a function of η barycenter, for test beam data (full circles) and simulation (open circles). The vertical dashed lines correspond to separations between S2 cells.*

4.1 Pion removal

The main problem for this analysis is the separation between electrons and pions around $\eta = 2.5$. Figure 16 shows the percentage of events remaining after the cut on the scintillator digital signal ($ADC_{pion} < 380$ ADC counts), located behind the calorimeter. When the separation is effective, pions ($\sim \frac{1}{3}$ of the events) can be removed (purity of more than 90 %). However around the crack, the cut removes electrons as well as pions because electrons still have most of their energy after passing through the calorimeter (where they deposit only 10% of their energy, cf. Figure 14).

Because of this problem, we used only the calorimeter response to separate electrons from pions, out of the region $\eta_{bar} = [2.49, 2.51]$, and we apply a cut $E_{tot} \geqslant 80$ GeV. No cut is applied in the region $\eta_{bar} = [2.49, 2.51]$.

The same selection is done in simulation. To obtain a better comparison with test beam data, 100 GeV pions[10] have been simulated in the crack region and added to the electrons (with the same proportion as for the 100 GeV beam).

4.2 Comparison between test beam data and simulation

Figure 17 shows the total energy as a function of η_{bar} for test beam data and simulation. Main differences are:

[10]No precise pion energy measurement was available so a 100 GeV default value was used.

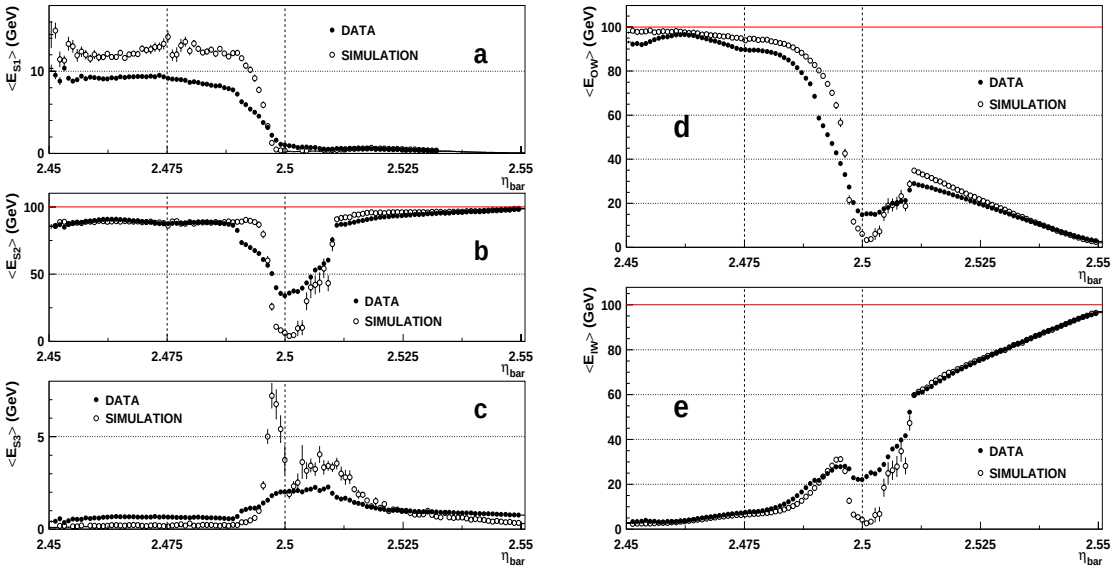

Figure 18: *a-c) Sampling energy and d-e) outer wheel and inner wheel energy as a function of η barycenter, for test beam data (full circles) and simulation (open circles). Vertical dashed lines correspond to cell separations.*

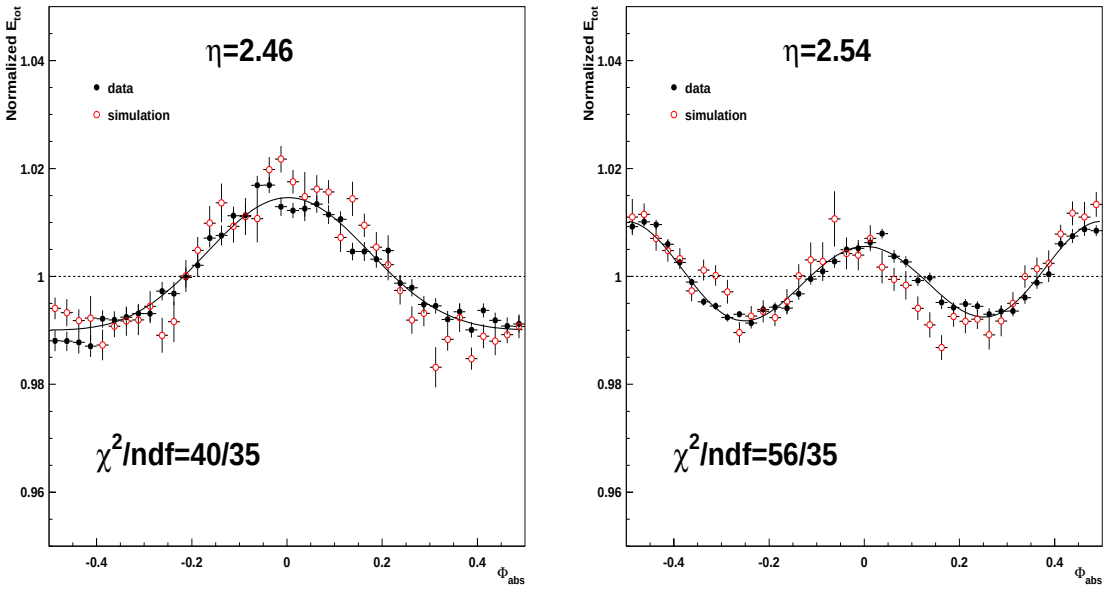

Figure 19: *φ-modulation at η=2.46 and η=2.54, for simulation and test beam data.*

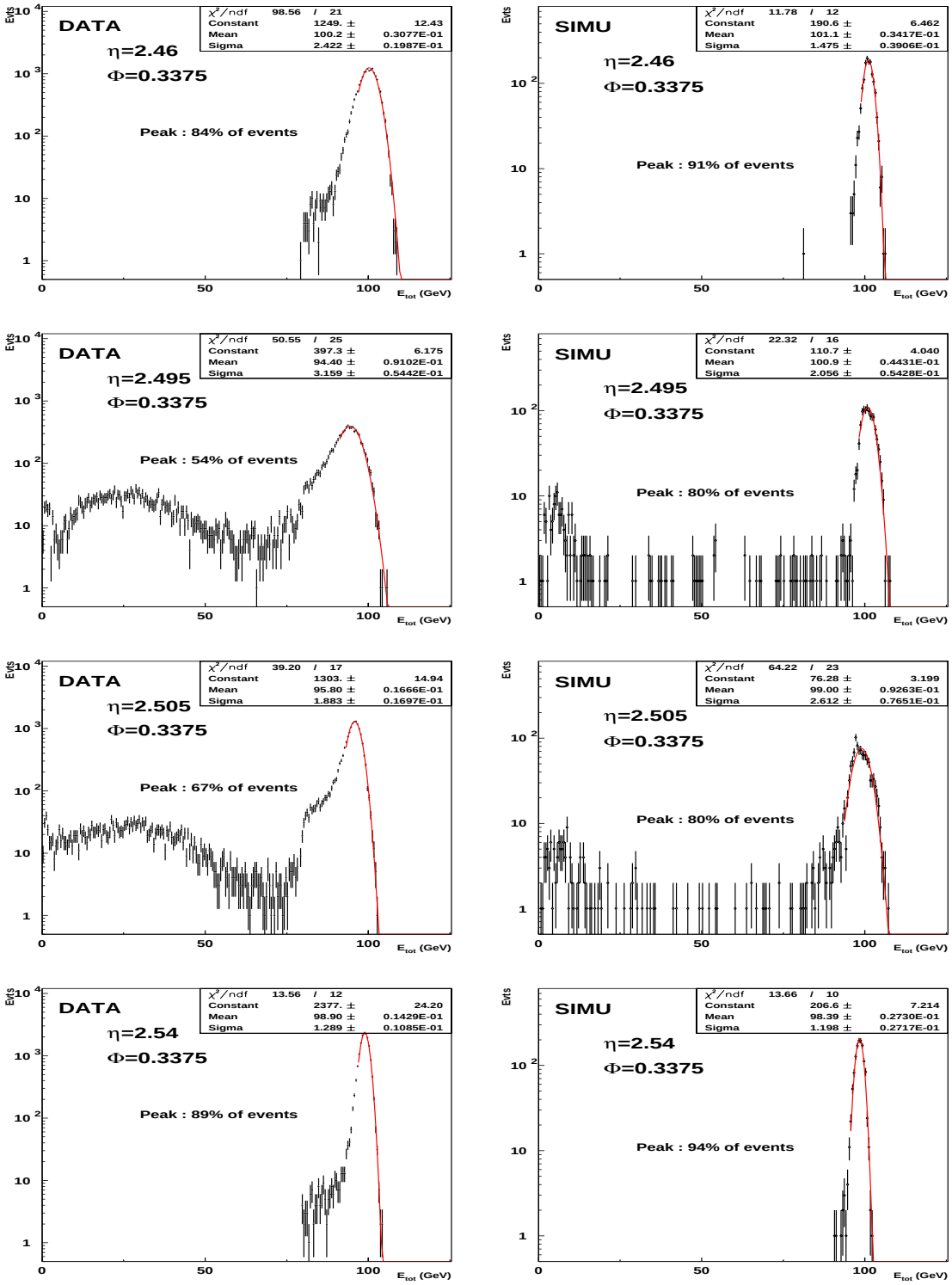

Figure 20: *Total energy distribution at four η positions for test beam data (on the left) and simulation (on the right). The gaussian fit on the peak close to the beam energy is given as well as the percentage of events on this peak.*

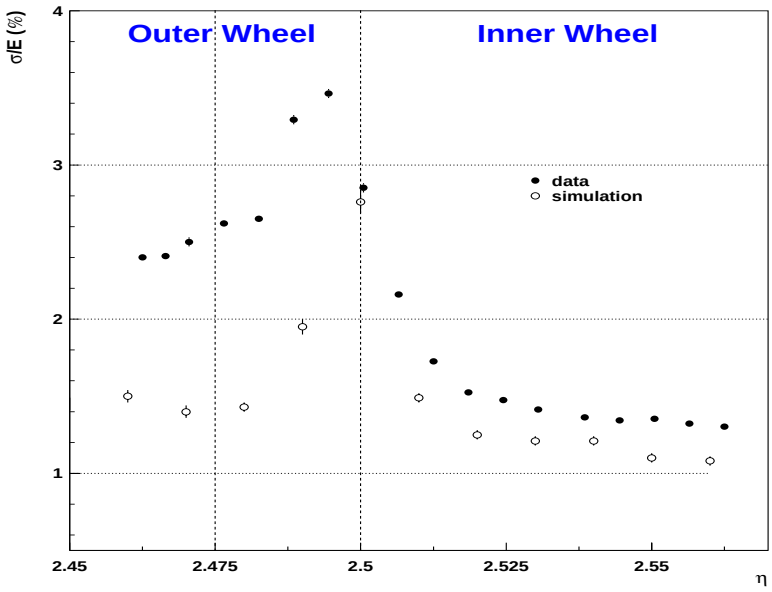

Figure 21: *Energy resolution as a function of η, for simulation and test beam data (beam spread has been subtracted) at 100 GeV.*

1. in the outer wheel: unexpected energy drop near $\eta = 2.475$ for test beam data (in view of the chosen large cluster). Simulation gives a flat energy response.

2. in the crack: smaller energy loss for data ($\sim 60\%$ at $\eta = 2.5$) than for simulation ($\sim 90\%$ at $\eta = 2.5$). This comes from uncertainties on pion simulation and possible non projectivity of the beam.

3. in the inner wheel: difference in the rising edge far from the center of the S2 cell.

To better understand these differences Figure 18 shows the energy per sampling (a-c) and per wheel (d-e). Effects labelled 1 and 3 in the upper list can be explained by the energy deposit in S2 cells of the outer wheel. This might be due to unsufficient grounding at η=2.5, not included in the simulation. It should also be noticed that the energy deposit in S1 is higher for simulation than for data (might be due to an inaccurate simulation of the matter in front of the calorimeter). Finally a different structure in the energy deposit in S3 cells is observed. However, in both case, the energy is increasing at $\eta = 2.5$ because of the later start of the electromagnetic shower. Typically a better agreement is found for the inner wheel than for the outer wheel.

4.3 Energy resolution

Because of the large cluster size, no η leakage corrections are applied. The ϕ-modulations are only corrected out of the range $\eta = [2.49, 2.51]$, because they are too much degraded

by the pions in this zone. Figure 19 shows a comparison between simulation and data of ϕ-modulation at $\eta = 2.46$ and $\eta = 2.54$, and a good agreement is found. Here, no degradation of the modulation is observed despite the presence of the crack.

Figure 20 shows the total energy distribution at 4 η values (2.46, 2.495. 2.505 and 2.54) for test beam data and simulation. Gaussian Fit, performed on the peak close to the beam energy, is represented, as well as the percentage of events in the peak. As expected, the energy resolution is degraded near the crack and more electrons are out of the peak.

Figure 21 shows the energy resolution as a function of η for simulation and test beam data. A good agreement is found in the inner wheel whereas in the outer wheel, the energy drop near $\eta = 2.475$ (cf. Figure 17) degrades the energy resolution in the data. As expected, the presence of the crack induces a degradation of the energy resolution ($\sim 100\%$) with the worst resolution at $\eta = 2.495$ ($\frac{\sigma}{E_{tot}} = 3.45\%$).

5 Conclusions

Complete uniformity scans were performed in the inner wheel of the EMEC module 0 with a 100 GeV positron beam. Results are shown for: *i*) one ϕ line in the η range [2.6,3.1], as well as in the crack region [2.45,2.55], and *ii*) several η lines in the region around η=2.65, 2.85 and 2.95. They are obtained using the last version of optimal filtering for the calibration signals, as well as for the physics data. Variation of inductance are corrected in η and ϕ in this analysis.

Concerning the inner wheel scan, main conclusions are:

1. η lateral leakage corrections suffers from the barycenter bias due to large S2 cell size.

2. ϕ-modulation, in good agreement with simulation including charge collection, can be fitted with a 3-parameter Fourier serie. Extracted coefficients can be parametrized as a function of η.

3. Energy resolution is around 1.2-1.3% after all geometrical corrections and beam spread subtraction.

4. After applying all corrections, energy dispersion is 0.61% for η scan and around 0.4% for the ϕ scans.

A 0.64% global constant term, compatible with expectations, can be extracted from these scans.

The study of the crack region ($\eta \sim 2.5$) is affected by the presence of pions (pion removal is not possible around $\eta = 2.5$ because electrons are not completely contained in the calorimeter). Despite this effect, that we tried to take into account in the simulation, we can conclude that:

1. The sensitive zone given by simulation is $\eta = 2.5 \pm^{0.004}_{0.004}$.

2. 60% (resp. 90%) of the total energy is lost in the crack zone for test beam data (resp. simulation).

3. Energy resolution is degraded by the presence of the crack by a factor ~ 2.

A possible solution to improve pion removal in this region is to put lead between calorimeter and scintillator.

Acknowledgements

We want to thank Emmanuel Monnier for carefully reading this manuscript, Calin Alexa for his help with simulation and Lionel Neukermans for providing the correction factors for inductance variation.

References

[1] ATLAS Collaboration, *ATLAS Liquid Argon Calorimeter Technical Design Report*, CERN/LHCC/96-41.

[2] P. Barrillon, F. Djama, L. Hinz and P. Pralavorio, *Uniformity scan in the Outer Wheel of the Electromagnetic End-cap Calorimeter*, ATL-LARG-2001-012

[3] A. Mirea, E. Nagy and J. Tóth, *Study of the optimum division of the electromagnetic calorimeter into two samplings at* $\eta > 2.5$, ATL-LARG-97-078.

[4] O. Martin, E. Monnier and S. Tisserant, *Update of some Geometrical Parameters for the ATLAS E.M. End-Cap Calorimeter*, ATLAS-LARG-96-047.

[5] P. Pralavorio and D. Sauvage, *Review of the crosstalk in the module 0 of the Electromagnetic End-cap Calorimeter*, ATL-LARG-2001-006.

[6] K. Elsener, *Short Introduction to the use of the H6 beam*,
http://sl.web.cern.ch/SL/eagroup/beams.html#h6

[7] D. Nicod, D. Zerwas and R. Zitoun, *EMTB User Guide*,
http://atlasinfo.cern.ch/Atlas/GROUPS/LIQARGON/TESTBEAM/emtbdoc.ps

[8] P. Barrillon, F. Djama, L. Hinz and P. Pralavorio, *Optimal Filtering in the Electromagnetic End-cap Calorimeter*. Note in preparation.

[9] B. Mansoulie and J. Schwindling, *Using Multi Layer Perceptrons in PAW*,
http://schwind.home.cern.ch/schwind/MLPfit.html

[10] L. Neukermans, P. Perrodo and R. Zitoun, *Understanding the ATLAS electromagnetic barrel pulse shapes and the absolute electronic calibration*. ATL-COM-LARG-2001-007

[11] F. Djama, L. Hervas and C.P. Marin, *Copper-Polyimide Multi-Layer Electrodes for the End-Cap Electromagnetic Calorimeter*, ATL-LARG-98-088.

[12] P. Barrillon, F. Djama, L. Hinz and P. Pralavorio, *Energy resolution of the Electromagnetic End-cap Calorimeter*. Note in preparation.